

Comparison of ring artifact correction methods for flat-detector CT

This article has been downloaded from IOPscience. Please scroll down to see the full text article.

2009 Phys. Med. Biol. 54 3881

(<http://iopscience.iop.org/0031-9155/54/12/018>)

View [the table of contents for this issue](#), or go to the [journal homepage](#) for more

Download details:

IP Address: 128.135.74.178

The article was downloaded on 16/02/2012 at 17:33

Please note that [terms and conditions apply](#).

Comparison of ring artifact correction methods for flat-detector CT

Daniel Prell, Yiannis Kyriakou¹ and Willi A Kalender

Institute of Medical Physics, University of Erlangen-Nürnberg, Henkestraße 91, 91052 Erlangen, Germany

E-mail: yiannis.kyriakou@imp.uni-erlangen.de

Received 17 October 2008, in final form 13 May 2009

Published 2 June 2009

Online at stacks.iop.org/PMB/54/3881

Abstract

In flat-detector CT, imperfect or defect detector elements may cause concentric ring artifacts due to their continuous over- or underestimation of attenuation values, which often disturb image quality. Especially due to the demand for high-spatial resolution images and the necessary pixel read-out without arbitrary pixel-binning, ring artifacts become more pronounced and the reduction of these artifacts becomes a necessity. We here present a comparison of two dedicated ring artifact correction methods for flat-detector CT, on the basis of different median and mean filterings of the reconstructed image but each working in different geometric planes. While the first method works in Cartesian coordinates, the second method performs a transformation to polar coordinates. Both post-processing methods efficiently reduce ring artifacts in the reconstructed images and improve image quality. The transformation to polar coordinates turned out to be a necessary step for efficient ring artifact correction, since correction in Cartesian coordinates suffers from newly introduced artifacts as well as insufficient correction of artifacts close to the center of rotation.

(Some figures in this article are in colour only in the electronic version)

1. Introduction

In flat-detector CT (FD-CT), reconstructed images are often disturbed by ring artifacts and thus prevent a proper diagnosis of the structures of interest, e.g., fine bone details or low contrast structures (Sijbers and Postnov 2004, Riess *et al* 2004). The artifacts are caused by imperfect detector elements, which throughout the scan process significantly under- or overestimate attenuation values. These discrepancies are noticed in the reconstructed image

¹ Author to whom any correspondence should be addressed.

Table 1. Symbols and abbreviations.

Nomenclature	
Symbols	
d_{RA}	Calculated ring artifact thickness
M_1	Radial median filter width in Cartesian coordinates
M_{Azi}	Azimuthal filtering in polar coordinates
M_{Rad}	Radial filtering in polar coordinates
$d_{u,v}$	Pixel size detector
$d_{x,y}$	Pixel size reconstructed image
R_F	Distance rotation-axis to focus
R_D	Distance rotation-axis to detector
T_{min}	Lower threshold for image segmentation
T_{max}	Upper threshold for image segmentation
T_{RA}	Second threshold for ring artifact segmentation
FD-CT	C-arm based CT using a flat-panel detector

as concentric ring-like artifacts which are superimposed onto the initial image and disturb the diagnostic quality of the images (Kinney 1989, Lai 2000). Post-processing correction methods and segmentation algorithms are also impaired in their performance.

The causes for the falsified pixel responses are manifold. They range from individual temperature instability and radiation damage to different scintillator thicknesses (Sijbers and Postnov 2004, Lai 2000). The effects become even more noticeable when high-resolution images are demanded, since the read-out of each pixel counts and no mean attenuation value over binned detector pixels is used for reconstructions (Sijbers and Postnov 2004). The ring artifacts in high-resolution images are more distinct and may disturb diagnostic images severely.

Different pre- and post-processing ring artifact correction algorithms were developed to diminish the effects of false pixel responses. Nevertheless, pre-processing algorithms based on flat-field corrections, moving detector arrays during acquisition and sinogram processing still do not sufficiently remove ring artifacts (Riess *et al* 2004).

More promising approaches are post-processing algorithms which operate directly on the reconstructed image. In this study, a comparison of two dedicated post-processing ring artifact correction algorithms was performed and evaluated in phantom studies and on clinical data, and their effectiveness and impact on image quality was investigated for different acquisition modes.

2. Materials and methods

Symbols and abbreviations used in this paper are summarized in table 1.

In this section, the basic ideas behind the two correction methods are explained. Both methods work with median and mean filterings of the reconstructed images to identify the ring artifacts and use simple image processing for correction. The first implemented correction method in Cartesian coordinates conforms to the algorithm published by Zellerhoff *et al* (2005). The second correction algorithm is based on the same principle ideas but uses a transformation of the reconstructed image to polar coordinates and adaptive, distance-dependent radial and azimuthal filtering methods.

2.1. Correction methods

A necessary pre-processing step, which both correction methods have in common, is a segmentation of the image with boundary conditions. Two thresholds (lower threshold T_{\min} , upper threshold T_{\max}) ensure that no new artifacts are induced by the correction algorithm. Without this segmentation, bone fractures or details with the same diameter as the actual ring artifacts would grow together during the correction process and the correction methods would overcorrect falsely as ring structures identified bone or low contrast structures. Additionally, *a priori* knowledge of the scanner geometry is used to estimate ring structure thicknesses and positions in the reconstructed image. The thresholded image thus becomes

$$f_{\text{Thres}}(x, y) = \{x, y \mid f_0(x, y) < T_{\max} \wedge f_0(x, y) > T_{\min}\}, \quad (1)$$

where $f_0(x, y)$ denotes the original image, T_{\max} is the upper threshold (bone threshold) and T_{\min} is the lower threshold (air threshold).

2.1.1. Ring correction in Cartesian coordinates (RCC). In summary, the correction process is divided into different steps as follows.

Radial median filtering. The first step involves the median filtering of the thresholded image $f_{\text{Thres}}(x, y)$ orthogonally to the artifact structure (radial direction), starting from the center of rotation. The thresholded image $f_{\text{Thres}}(x, y)$ is therefore sub-sampled, using $2 \cdot M_{\text{Rad}} + 1$ support points in a distance d_{RA} with an empirical filter width of $M_{\text{Rad}} = 15$, where d_{RA} corresponds to the expected circular artifact size. To calculate adequate support points in the radial direction, each coordinate of the sub-sampled image for $2 \cdot M_{\text{Rad}} + 1$ support points is calculated as

$$x_s = x_0 + (d_R - n \cdot d_{\text{RA}}) \cdot d_{x_e} \quad (2)$$

$$y_s = y_0 + (d_R - n \cdot d_{\text{RA}}) \cdot d_{y_e}, \quad (3)$$

where

$$dx = x - x_0 \quad (4)$$

$$dy = y - y_0 \quad (5)$$

$$d_R = \sqrt{dx^2 + dy^2} \quad (6)$$

$$d_{x_e} = dx/d_R \quad (7)$$

$$d_{y_e} = dy/d_R \quad (8)$$

with x and y being the coordinates of the original image pixel $f(x, y)$ to be filtered, dx and dy being the distances in the x - and y -direction respectively, d_R being the increment in the thus defined direction, and d_{x_e} and d_{y_e} being the corresponding increments in the subsampled x - and y -direction. For each subsampled image pixel $f_s(x_s, y_s)$, the next reliable image pixel of the original image $f(x, y)$ is chosen. After filling the $2 \cdot M_{\text{Rad}} + 1$ support points and sorting them ascendingly, the median value, which corresponds to the value of the support point M_{Rad} (middle entry), is used for the median filtered image $f_M(x, y)$. A mathematical calculation for the circular artifact size in pixels is given by

$$d_{\text{RA}} = \left(\frac{R_F}{R_D + R_F} \right) \cdot \frac{d_{u,v} \cdot b}{d_{x,y}}, \quad (9)$$

where R_F is the radius of the focus trajectory, R_D is the radius of the detector trajectory and $d_{u,v} = (du + dv)/2$ and $d_{x,y} = (dx + dy)/2$ denote the mean detector pixel size and the mean image pixel size, respectively. b accounts for detector pixel-binning during acquisition, where $b = 1$ for an unbinned detector, $b = 2$ for 2×2 binning and $b = 4$ for 4×4 binning. The maximal number of individual image pixels used for the median filtering complies with $2 \cdot M_{\text{Rad}} + 1$ image pixels.

The median filtered image is hence defined as a convolution with the global, median filter $M_{M_{\text{Rad}}, d_{\text{RA}}}$ and becomes

$$f_M(x, y) = f_{\text{Thres}}(x, y) \otimes M_{M_1, d_{\text{RA}}}, \quad \forall x, y. \quad (10)$$

Identifying the ring artifacts. To identify ring artifact structures, a calculation of the difference between the median filtered image and the thresholded image is performed as given by

$$\Delta f(x, y) = f_{\text{Thres}}(x, y) - f_M(x, y), \quad \forall x, y, \quad (11)$$

with $f_{\text{Thres}}(x, y)$ being the thresholded image and $f_M(x, y)$ being the median filtered image.

After subtraction, the difference image contains the perturbing ring structures but might also still contain mistakenly segmented bone edges. A second thresholding of the difference image with T_{RA} aims to ensure that only ring artifact structures are present. T_{RA} is chosen such that ring artifact structures pass the filtering while bone structures are excluded. Typical values for T_{RA} range from 300 to 100 HU. In this paper, an empirical value of 250 HU for T_{RA} was chosen.

Since the difference image also contains noise structures, low-pass filtering in the azimuthal direction aims to provide a noise-reduced image which only contains artifact structures. Filtering in the azimuthal direction becomes more sophisticated close to the center of rotation compared to filtering in the outer regions since there are less image pixels available for an adequate filtering, and thus the filter widths have to be adjusted. The difference image is therefore divided into an inner and outer region along the radial direction, defined by d_{IAP} , starting from the center of rotation to the point most distant from it. d_{IAP} is set to an empirical value of 15% of the maximal expected radius of the image, measured from the center of rotation. Again, the positions for $2 \cdot M_{\text{Azi}} + 1$ support points are calculated in the azimuthal direction in a distance d_{AZ} for the subsampled image. The low-pass filter itself complies thus with a mean filter with a filter width of $M_{\text{Azi}} = 10$, using $2 \cdot M_{\text{Azi}} + 1$ support points. d_{AZ} depends on the image region of the pixel to be filtered, and is therefore empirically defined as

$$d_{\text{AZ}} = \begin{cases} 1^\circ & \text{for the inner region} \\ 0.5^\circ & \text{for the outer region,} \end{cases} \quad (12)$$

where the inner and outer regions are defined as $0 < r \leq d_{\text{IAP}}$ and $d_{\text{IAP}} < r \leq d_{\text{max}}$, respectively. d_{max} is defined as the maximal elongation in the radial direction, starting from the center of rotation. For each position of the subsampled image, the nearest reliable image pixel values are chosen for the $2 \cdot M_{\text{Azi}} + 1$ support points. The distinction between the inner and outer regions of the image is a necessary step to ensure that each of the $2 \cdot M_{\text{Azi}} + 1$ support points belongs to an individual image pixel but also that the support points are close enough together without skipping image pixels. The latter ensures that partial circular artifacts are not smeared in areas exceeding the actual artifact.

Correcting the initial image. Ring artifact structures appear as superimposed structures on the initial image (Kinney 1989, Zellerhoff *et al* 2005). Subtraction of the ring artifact image from the initial image results in an artifact-free image as given by

$$f_{\text{corr}}(x, y) = f_0(x, y) - \Delta f(x, y), \quad \forall x, y, \quad (13)$$

where $f_{\text{corr}}(x, y)$ denotes the corrected image. Ring artifacts therefore are regarded as a simple offset to the initial image. This global correction procedure has minimum impact on the image resolution (Sijbers and Postnov 2004).

2.1.2. Ring correction in polar coordinates (RCP). Since correction in Cartesian coordinates becomes more difficult the closer one gets to the center of rotation, correction in polar coordinates is expected to simplify both median filters and reduce the number of default parameters. The correction algorithm in polar coordinates involves the same steps as mentioned above except that the identification of the ring structures is performed in polar coordinates. Therefore, the initial image is transformed into polar coordinates as described by Sijbers and Postnov (2004). Conversion to polar coordinates is done by using

$$f_{\text{pol}}(r, \vartheta) = \tilde{T} * f_{\text{cart}}(x, y), \quad \tilde{T} := \begin{pmatrix} r = \sqrt{x^2 + y^2} \\ \vartheta = \arctan \frac{y}{x} \end{pmatrix}, \quad (14)$$

where \tilde{T} denotes the transformation matrix from Cartesian to polar coordinates. For each r and ϑ , $f_{\text{pol}}(r, \vartheta)$ is calculated by using nearest neighbor interpolation.

There are several advantages of working in polar coordinates. Polar coordinates allow a simple distance-dependent, linear filtering of the initial image. Both radial and azimuthal filter widths are adjusted depending on the distance r to the center of rotation, making

$$M_{\text{Rad}} = M_{\text{Rad}}(r) \quad (15)$$

$$M_{\text{Azi}} = M_{\text{Azi}}(r) \quad (16)$$

a function of r , with M_{Rad} and M_{Azi} being the filter widths in the radial and azimuthal directions, respectively. The polar coordinates image is divided into three regions in the radial direction (inner, middle and outer regions), each with a specific filter width M_{Rad} , starting with a filter width of $3/3 \cdot M_{\text{Rad}}$ for the outer, $2/3 \cdot M_{\text{Rad}}$ for the middle and $1/3 \cdot M_{\text{Rad}}$ for the inner region, respectively. M_{Rad} was set to the same value as for the correction in Cartesian coordinates ($M_{\text{Rad}} = 15$).

The azimuthal direction is also divided into three regions, each with a specific filter width, where again the filter width was set to $3/3 \cdot M_{\text{Azi}}$ for the outer, $2/3 \cdot M_{\text{Azi}}$ for the middle and $1/3 \cdot M_{\text{Azi}}$ for the inner region. M_{Azi} was set to an empirical value of 40 pixels in polar coordinates, corresponding to an angular degree of approximately 0.8° .

In the final step, back transformation of the artifact image into Cartesian coordinates yields the ring structures in Cartesian coordinates. This artifact image is also simply subtracted from the initial image. The back transformation is performed by using the inverse transformation matrix \tilde{T}^{-1} ,

$$f_{\text{cart}}(x, y) = \tilde{T}^{-1} * f_{\text{pol}}(r, \vartheta), \quad \tilde{T}^{-1} := \begin{pmatrix} x = r \cdot \cos \vartheta \\ y = r \cdot \sin \vartheta \end{pmatrix}. \quad (17)$$

Figure 1 shows the correction algorithm at a glance as a flow chart and figure 2 shows the correction process exemplarily for RCP by means of actual clinical data and the different processing steps.

2.2. Phantoms and evaluation

Measurements were performed on a C-arm CT system (Artis Zeego, Siemens Healthcare, Forchheim, Germany) with a large flat detector (FD) and a detector size of $40.0 \times 30.0 \text{ cm}^2$ (pixel size of $154 \mu\text{m}$, 1×1 binning, $308 \mu\text{m}$, 2×2 binning, $616 \mu\text{m}$, 4×4 binning, CsI(Tl))

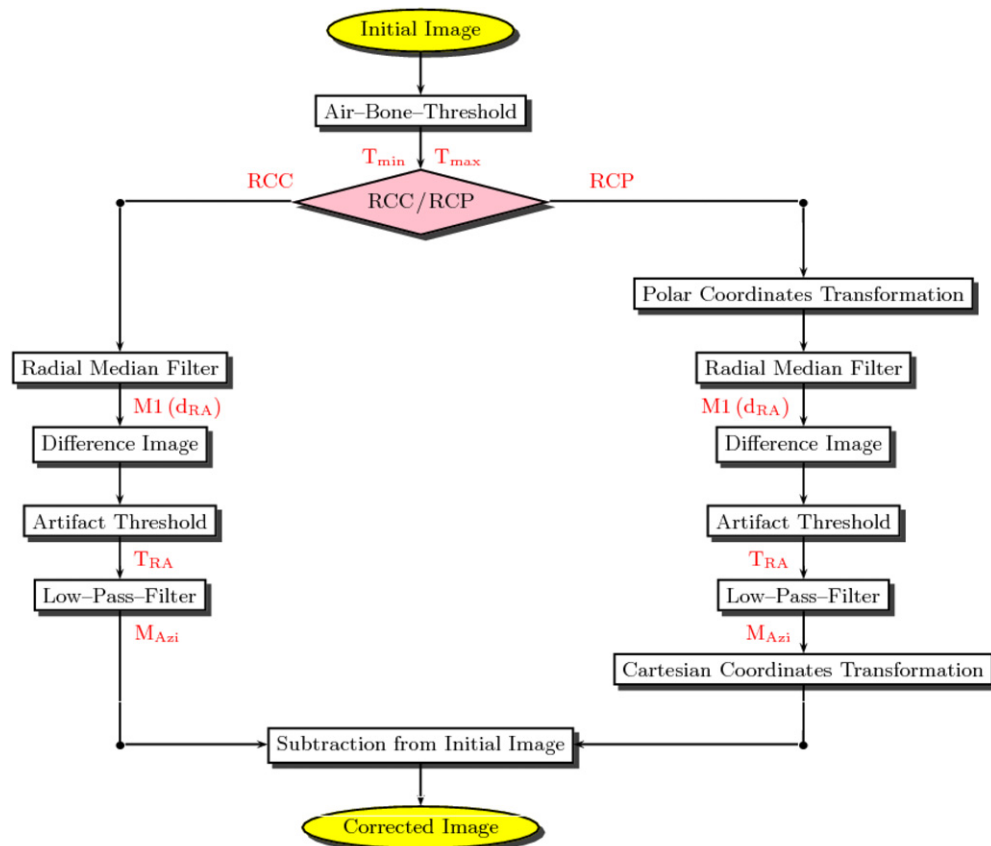


Figure 1. Flow chart of the two correction algorithms: (RCC)—ring correction in Cartesian coordinates; (RCP)—ring correction in polar coordinates.

a:Si). Standard Feldkamp (FDK) (Kalender 2005, Feldkamp *et al* 1984) reconstruction with a smooth kernel was used for image reconstruction combined with Parker weighting (Parker 1982) for partial scans.

In a water phantom (diameter $d_{H_2O} = 20$ cm), standard deviation and CT values were measured in central and peripheral ROIs according to the IEC 61223-3-5 standard. Additionally, an anthropomorphic skull phantom and clinical (head examination) and pre-clinical (examination of a free-breathing rat) data were used for validating effectiveness and precision of both methods in order to cover a variety of cases.

To evaluate the influence of different scan modes and pixel-binnings on ring characteristics and on the effectiveness of our correction methods, the correction algorithms were applied to measurements with different angular ranges, i.e., partial scan (an angular range of 218°) and full scan (an angular range of 360°) to investigate the influence of different scan modes on ring artifact characteristics. For the same reason, we varied the detector pixel-binning from 4×4 to 2×2 and 1×1 binning and investigated the influence by means of the water phantom. Acquisition using 1×1 pixel-binning was measured with a 218° partial scan and an angular increment of 2.0° (176 projections) due to data read-out limitations of the flat detector. 2×2 and 4×4 pixel-binning was measured with a 218° partial scan and an angular increment of

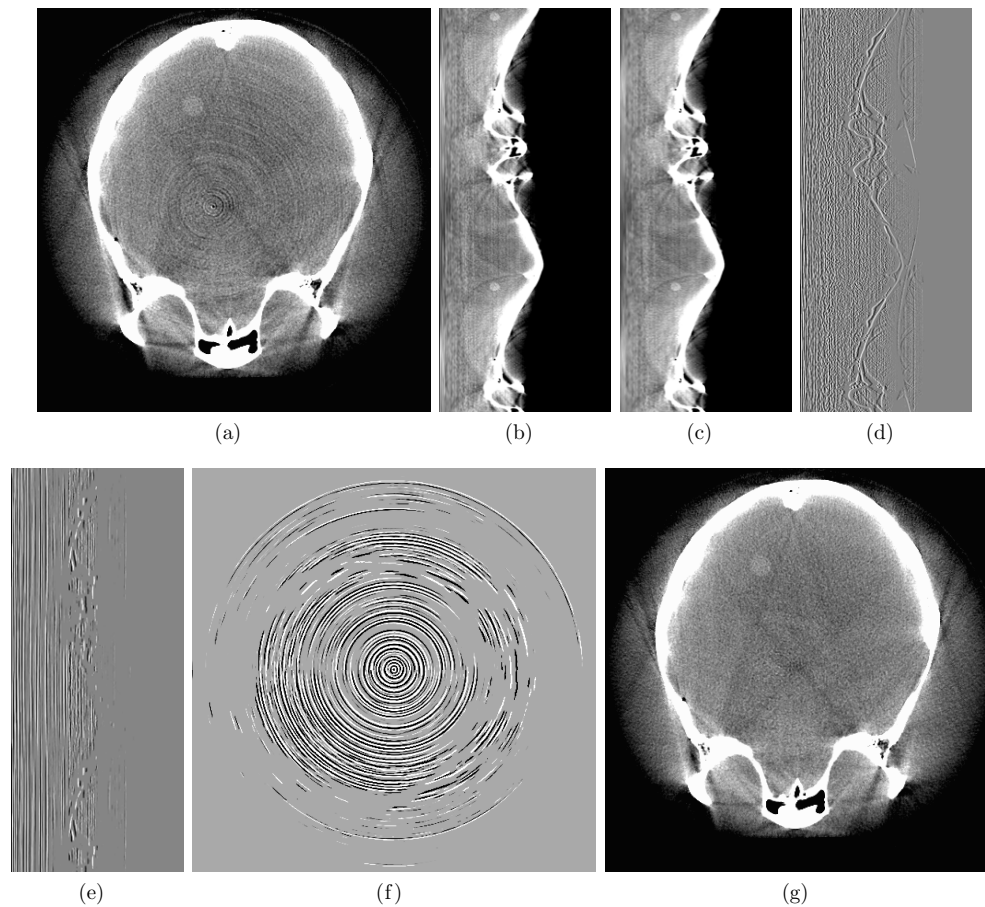


Figure 2. The correction process shown exemplarily for polar space correction. To prevent information losses, the polar space transformation is performed for $360^\circ \pm 90^\circ$: (a) the initial image (C-100/W300); (b) the transformation into polar coordinates (C-100/W300); (c) the radial median filter $M1_{dRA}$ image (C-100/W300); (d) the difference image (C0/W25); (e) the image after low-pass filtering with $M_{Rad}(r)$, $M_{Azi}(r)$ (C0/W25); (f) the correction image (C0/W25); (g) the corrected image (C-100/W300).

0.4° (496 projections). Clinical and pre-clinical data were measured using the 2×2 mode, which is the current standard. Note that due to the different binning settings and an automatic exposure control (AEC) system, the dose used for imaging could not be kept constant, since tube current and tube voltage were adapted by the system's AEC.

3. Results and discussion

Thresholding of the initial image can be performed completely automatically. Empirical values of $T_{min} = -300$ HU and $T_{max} = 300$ HU achieved good results during the correction process. An adjustment to specific image settings was not necessary. Hence, correction of all data sets could be performed with these global parameters while completely excluding bone structures in the difference image. Consequently, our correction methods can be used

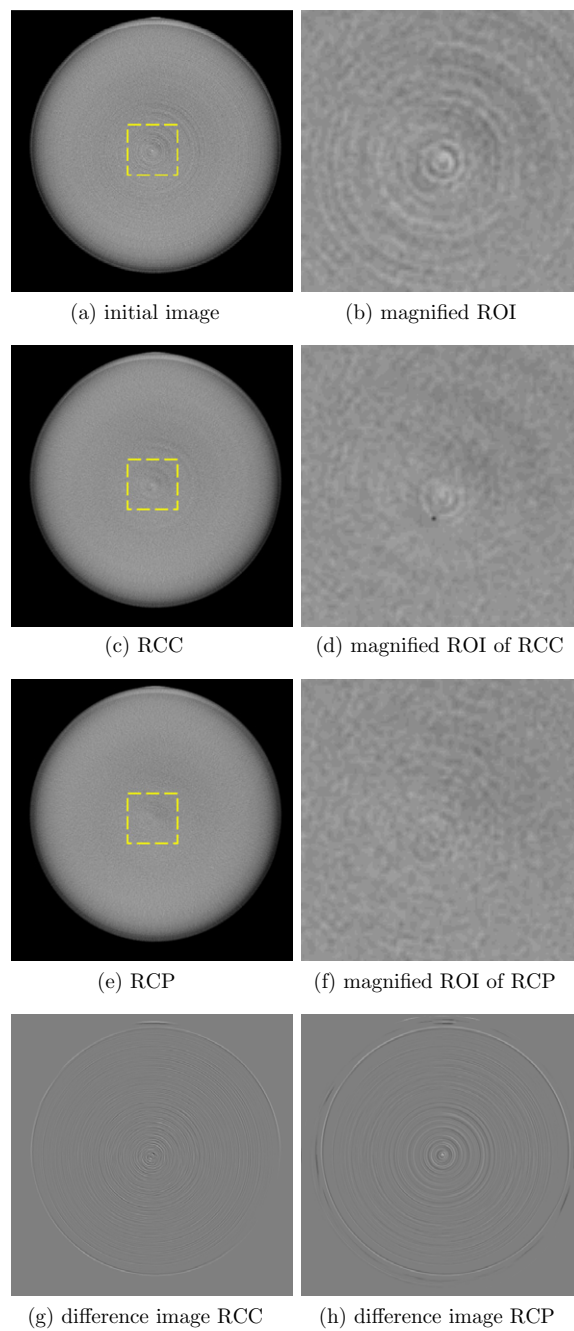


Figure 3. Water phantom: (a) initial image, (b) magnified ROI of the initial image, (c) RCC, (d) magnified ROI of RCC, (e) RCP and (f) magnified ROI of RCP (C-160/W400). For RCC images, new artifacts due to the correction algorithm appear close to the center of rotation. RCP completely removes these new artifacts. (g) Difference image for RCC; (h) difference image for RCP (C0/W200).

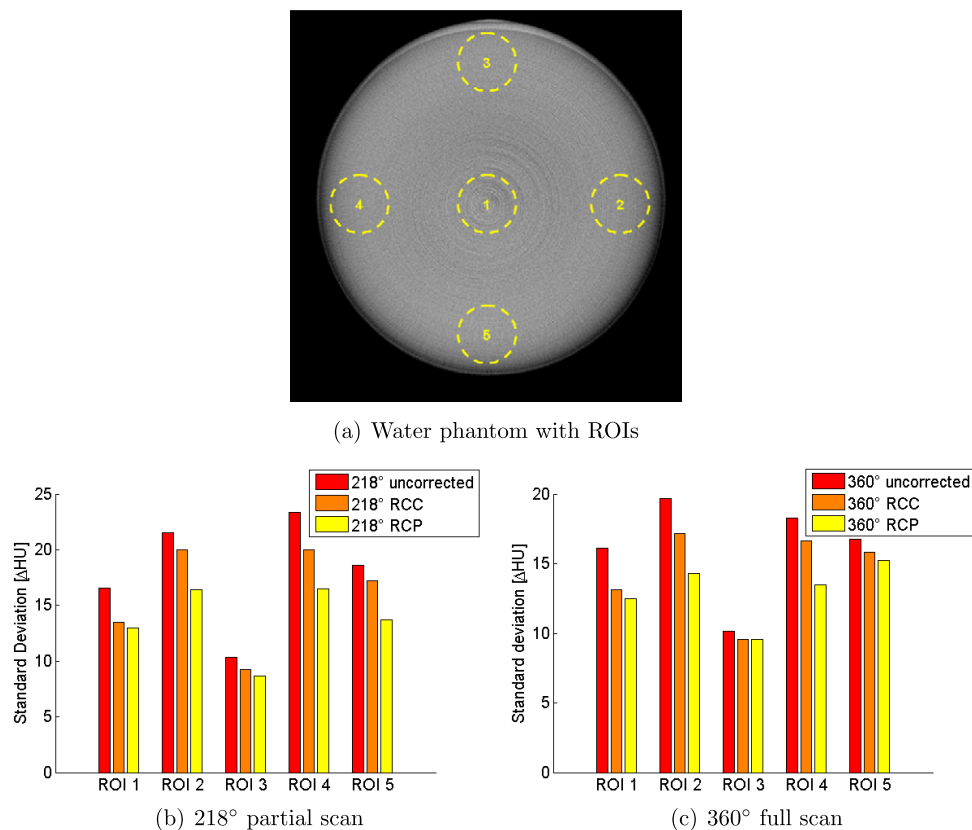


Figure 4. Water phantom with regions of interest for evaluation (a) and the corresponding standard deviation plots for both acquisition modes (b) and (c). After correction, the decrease in image noise is evident from the decreasing standard deviations (C-160/W450).

automatically. Only the correction of high-contrast images with bony structures might require an adjustment of the global thresholds.

Figure 3(a) shows the uncorrected, initial image compared to the images corrected by RCC and RCP (figures 3(b) and (c)) of the measured water phantom. Figures 3(d)–(f) show the difference images for both correction methods in comparison to the initial image. A more precise look at the magnified regions in figures 3(g)–(h) indicates the newly induced artifacts caused by azimuthal filtering (figure 3(f)) used by the RCC method. Applying the transformation into polar space (RCP), figure 3(h), clearly yields a more efficient reduction in ring artifacts, even at the center of rotation. Figure 4 illustrates that the standard deviations corresponding to image noise in ROI 1, ROI 2, ROI 3, ROI 4 and ROI 5 (figure 4(a)) are reduced by up to typically 18% for RCC and 22% for RCP. Ring artifact-deteriorated areas are corrected and it results in an increase of homogeneity in CT values (see ROI 1, ROI 2, ROI 3, ROI 4 and ROI 5 in figures 3(b) and (c)). Note that due to inhomogeneous CT values caused by scatter, beam hardening and other artifact sources, cupping and capping artifacts are introduced in the reconstructed images. Although correction algorithms included in the dedicated reconstruction software corrected for artifacts, there remains some inhomogeneity of the CT value distribution. This also results in an inhomogeneous noise distribution in the image. For example, ROI 3 always showed a significantly lower noise value. In the

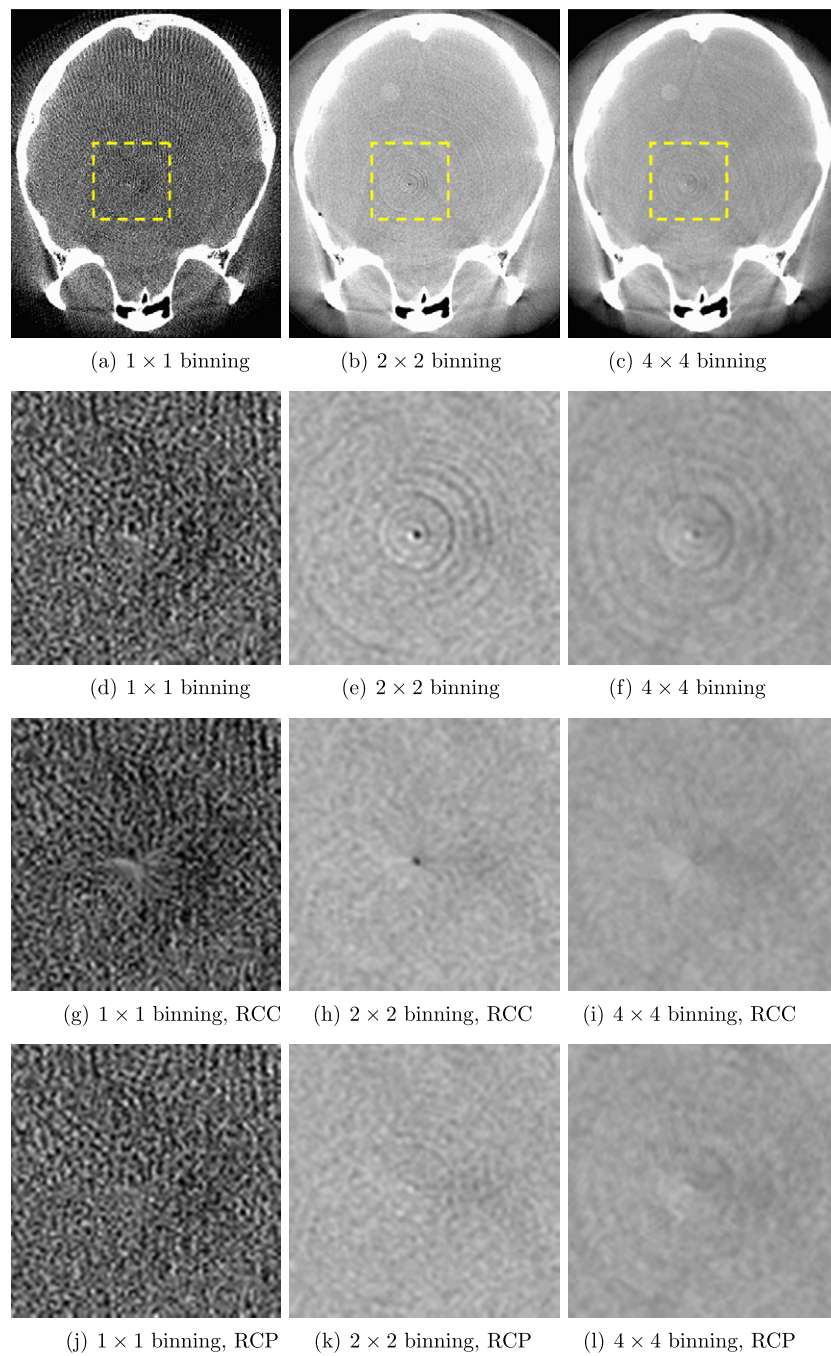


Figure 5. Human skull phantom measured with different pixel-binnings for a partial scan (218°) of (a) 1×1 , (b) 2×2 , (c) 4×4 binning and their corresponding magnified ROIs (d)–(f) for the uncorrected case. The corresponding corrected magnified ROIs are shown in (g)–(i) and (j)–(l) for the RCC and RPC algorithms, respectively (C0/W1000).

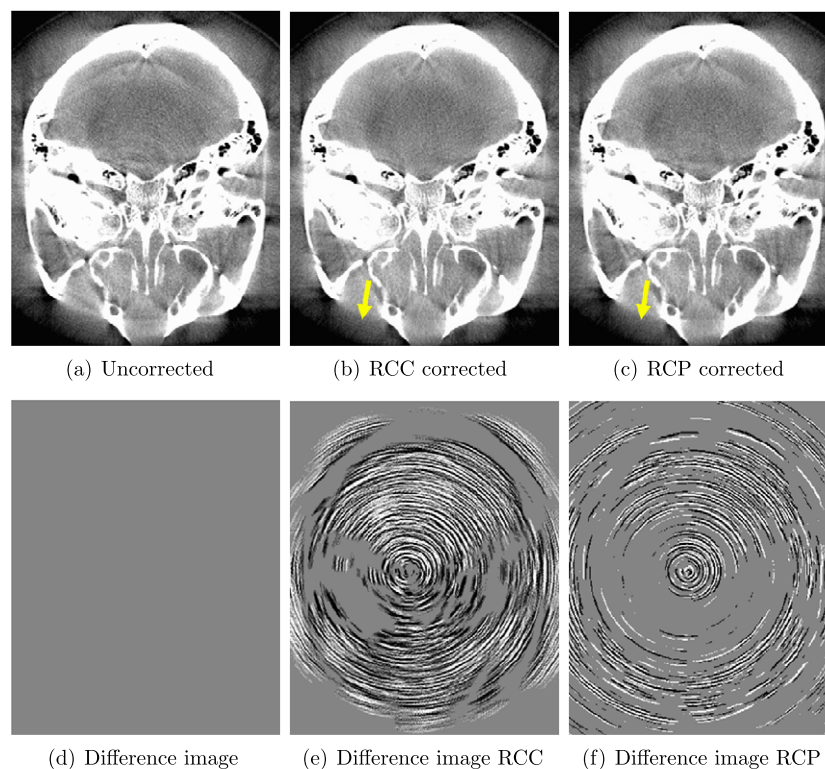


Figure 6. Skull phantom (a) uncorrected, (b) RCC corrected and (c) RCP corrected (C0/W1000). The corresponding difference images for the (d) uncorrected, (e) RCC corrected and (f) RCP corrected image (C0/W20) are shown below. No object structures are visible in the difference images, which implies that spatial resolution was preserved.

reconstructed image, local evaluations of image noise in ROIs constitute the standard metric throughout the literature (Sijbers and Postnov 2004, Riess *et al* 2004), although these artifact sources have a global impact on noise distribution (Kalender 2005).

The influence of different scan modes expresses itself in distinct ring structures. While a 218° scan shows partially opened circles, a 360° scan results in fully closed circles. For both acquisition modes, the same parameter settings for correction were retained. Figures 5(a)–(c) show the influence of different pixel-binnings on ring structures in the reconstructed image. With increasing pixel-binning and thus decreasing spatial resolution, ring structures become less distinct due to the averaging of pixel arrays. The magnified ROIs in figures 5(d)–(f) indicate the disappearing of single-ring structures caused by the binning algorithm. According to Kalender (2005), image noise σ for isotropic spatial resolution is inversely proportional to the square of the sampling distance $\Delta\xi$ and since $\sigma \propto 1/(b \cdot \Delta\xi)^2 \propto 1/b^2$ also inversely proportional to the square of the pixel-binning b . For 1×1 binning in figures 5(a) and (d), the resulting image noise is of a magnitude 10 higher than the distinct ring structures and prevents a clear detection.

As mentioned before, the applied post-processing correction algorithms have minimal impact on resolution (Sijbers and Postnov 2004). CT values in the reconstructed image are either raised or lowered by our correction algorithm, but no filtering or smoothing is applied to the image. Figure 6 illustrates this effect by means of the difference images between

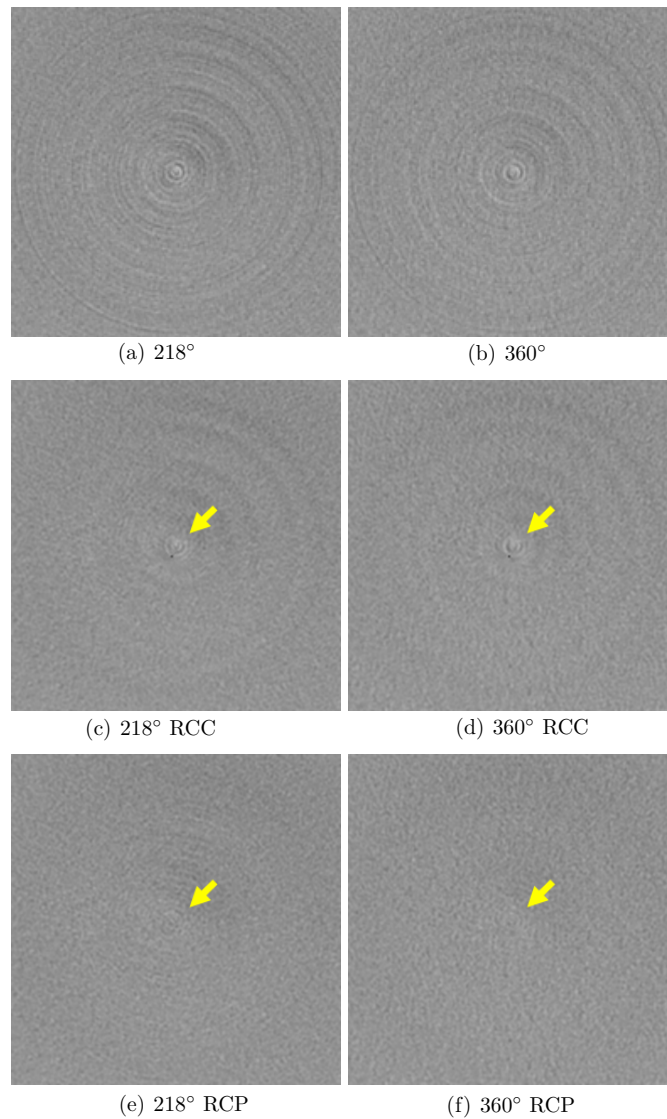


Figure 7. Magnified image centers for the water phantom for (a) 218° uncorrected, (b) 360° uncorrected, (c) 218° RCC, (d) 360° RCC, (e) 218° RCP and (f) 360° RCP. Newly induced artifacts due to azimuthal filtering (arrow) in Cartesian space are visible in the center of rotation for RCC images. RCP minimizes those artifacts (C-160/W450).

corrected and uncorrected images (figures 6(a)–(f)). Our thresholdings ensured the exclusion of bone and air structures. No structures other than ring structures are visible. Nevertheless, figure 6(e) shows a more emphasized correction in the image center and less on the outer parts of the image. This effect is due to the constant filter width M_{Azi} . Although the reconstructed image is split into two regions, filtering close to the center of rotation becomes very strong. In the outer regions, it is relatively weak and ring artifacts can still remain (see the arrow in figure 6(e)). This effect can be diminished by using the RCP algorithm. Figure 6(f) shows a

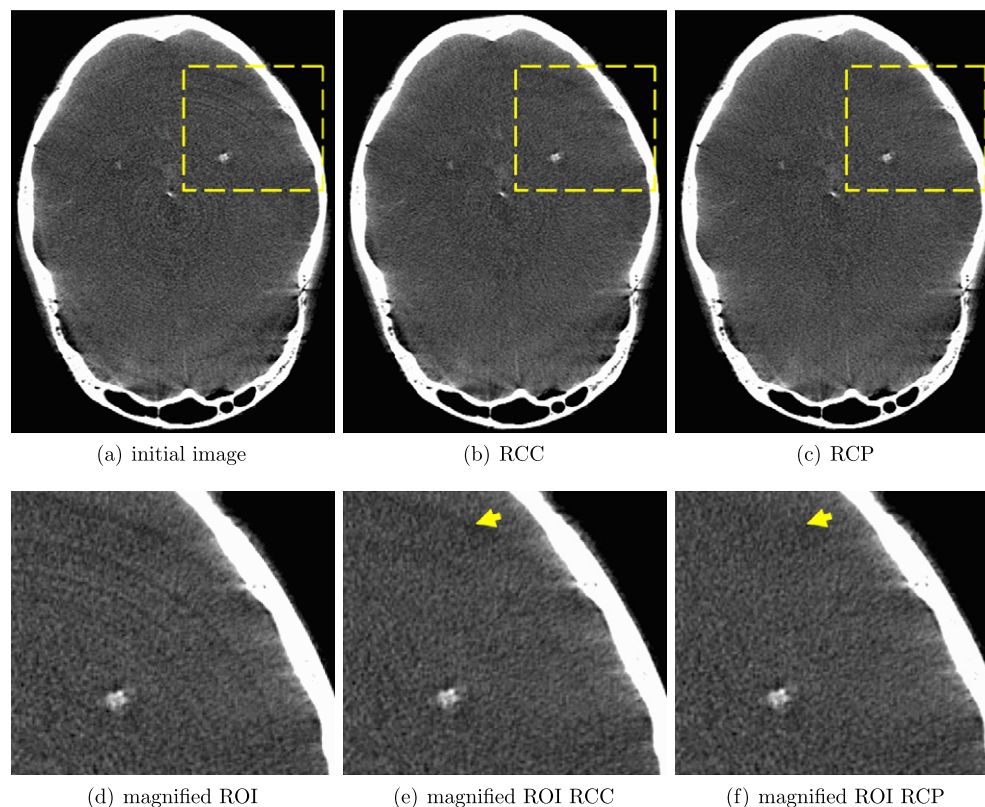


Figure 8. Head scan: (a) initial image, (b) RCC, (c) RCP (C160/W580) and the corresponding magnified regions (d) initial image, (e) RCC, (f) RCP. The magnified regions show the different modes of action of the correction algorithms. While ring artifacts still remain after applying RCC, correction with RCP corrects more efficiently (C160/W580).

constant correction of ring artifacts, independent of the image region and a notable reduction even in outer regions (see the arrow in figure 6(f)).

The magnified regions of the initial images for the measured water phantom are illustrated in figures 7(a) and (b). Figures 7(c) and (d) show little difference in artifact correction using RCC for either a 218° or a 360° scan mode. However, RCP indicates the influence of ring structure characteristics on the correction process. While figure 7(e) (218°) still shows slight ring structures in the corrected image, figure 7(f) for a 360° scan mode reduces remaining artifacts to a minimum. This influence is mostly due to lower image noise for 360° full scans. If image noise is close to the magnitude of the ring artifacts, pre-processing median filtering can eliminate these structures before detection.

By applying both correction methods to clinical data, the ring structures in the areas previously disturbed by ring artifacts are largely reduced (see figures 8(a) and 9(a) (uncorrected) compared to figures 8(b) and (c) and figures 9(b) and (c) (corrected)). Figures 8(d)–(f) and 9(d)–(f) also show that fine details, i.e., bone structures or low-contrast objects, are not influenced by either correction algorithms. The visibility of low-contrast structures is also improved after correction as shown in the corresponding magnified regions in figures 8(d)–(f) of a head scan and in figures 9(d)–(f) of a rat thorax scan (visible motion

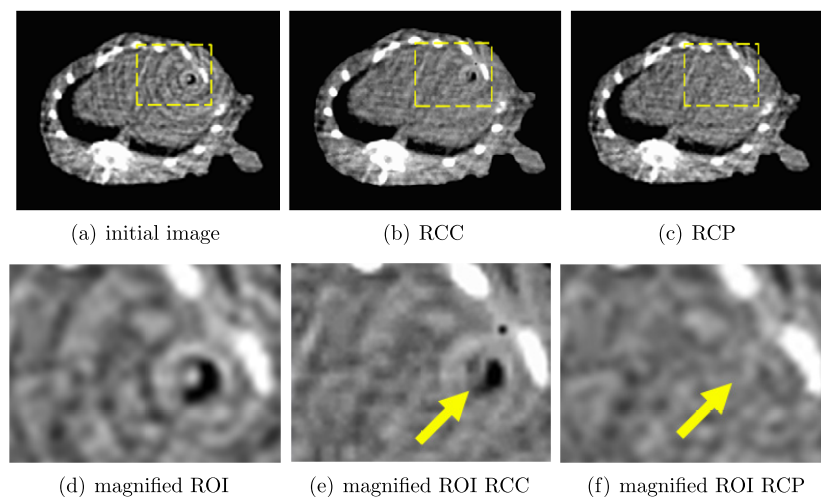


Figure 9. FD-CT scan of a rat thorax scan: (a) initial image, (b) RCC, (c) RCP (C260/W490) and the corresponding magnified regions (d) initial image, (e) RCC, (f) RCP. The magnified regions indicate the superiority of our RCP to RCC since artifacts close to the center of rotation are reduced more (C260/W490).

artifacts are caused by the respiration of the living rat). Figures 8(e) and (f) illustrate the difference in artifact removal between RCC and RCP. While RCC still retains slight ring artifacts, RCP minimizes the appearance of these ring structures in the corrected image. The same is shown for figures 9(e) and (f). Especially close to the center of rotation, the effectiveness of RCC is limited. Yet RCP is able to restore the information and allows us to correct even at the center of rotation.

Figures 9(b) and (e) also show the introduction of new artifacts due to azimuthal filtering in Cartesian space. Close to the center of rotation, correction is insufficient and additionally introduces new, streak-like artifacts, as can also be seen in figure 3(b). Nevertheless, as figures 8(c) and 9(c) show, using RCP for correction, the introduction of new artifacts is limited.

The limitations of RCC close to the center of rotation and at outer regions are due to the constant filter widths in these areas. While filtering close to the center of rotation simply does not provide enough image pixels for filtering, streak-like artifacts appear due to the falsified filtering. The only partial removal of circular artifacts in the outer regions is also due to the effect of fixed filter widths. Areas close to the maximal elongation of the image are due to the very low chosen filter widths for RCC. RCP does not encounter these problems; the next neighbor interpolation used during coordinate transformation ensures the availability of sufficient image pixels for filtering.

A comparison of both methods in terms of computation times shows that transformation into polar coordinates needs additional time for calculations. Since filtering in the radial and azimuthal directions of the RCP method is distance dependent, adjustment of the filter width almost doubles the correction time for the filtering itself. The most time-consuming correction step remains the calculation of the transformation matrix between the two coordinate systems. Thus, correction in polar space expands post-processing correction by up to 200% compared to correction in Cartesian space.

4. Conclusions

We compared two ring artifact correction methods, on the basis of the same principles of different median filterings and thresholdings but working in different geometric planes. Both methods reduce ring artifacts in FD-CT reconstructed images while keeping the desired high resolution of FD-CT. In conclusion, the most promising results were achieved by using the correction in polar coordinates. In every studied case, the correction was superior compared to the correction in Cartesian coordinates and should be the first choice. Low-contrast visibility is improved and images disturbed by ring artifacts can be well restored. The introduction of new artifacts due to the correction process has low impact on image quality. Nevertheless, they can be excluded by correcting in polar space despite the longer computation times. Nevertheless, longer computational times can be reduced by using acceleration techniques (Schiwietz *et al* 2007).

References

- Feldkamp L A, Davis L C and Kress J W 1984 Practical cone-beam algorithm *J. Optical Society America A* **1** 612–9
- Kalender W A 2005 *Computed Tomography* 2nd edn (Muenchen: Publicis MCD Verlag)
- Kinney J 1989 X-ray microtomography on beamline X at SSRL *Rev. Sci. Instrum.* **60** 2471–4
- Lai C-M 2000 Progressive correction of ring artifacts in a computed tomography system *US Patent* 6115445
- Parker D L 1982 Optimal short scan convolution reconstruction for fanbeam CT *Med. Phys.* **9** 254–7
- Riess T, Fuchs T and Kalender W A 2004 A new method to identify and to correct circular artifacts in x-ray CT images *Phys. Medica* **2** 43–55
- Schiwietz T, Bose S, Maltz J and Westermann R 2007 A fast and high-quality cone beam reconstruction pipeline using the GPU *Med. Imaging 2007; Proc. SPIE* **6510** 65105H
- Sijbers J and Postnov A 2004 Reduction of ring artefacts in high resolution micro-CT reconstructions *Phys. Med. Biol.* **49** 247–53
- Zellerhoff M, Scholz B, Ruehrnschopf E-P and Brunner T 2005 Low contrast 3D-reconstruction from C-arm data *Med. Imaging 2005; Proc. SPIE* **5745** 646–55